

# Silicon oxide-niobium oxide mixture films and nanolaminates grown by atomic layer deposition from niobium pentaethoxide and hexakis(ethylamino) disilane

Kaupo Kukli,<sup>1,\*</sup> Marianna Kemell,<sup>1</sup> Mikko J. Heikkilä,<sup>1</sup> Helena Castán,<sup>2</sup> Salvador Dueñas,<sup>2</sup> Kenichiro Mizohata,<sup>3</sup> Mikko Ritala,<sup>1</sup> Markku Leskelä<sup>1</sup>

<sup>1</sup>*Department of Chemistry, University of Helsinki, P.O. Box 55, FI-00014 Helsinki, Finland*

<sup>2</sup>*Department of Electronics, University of Valladolid, Paseo Belén, 15, 47011 Valladolid, Spain*

<sup>3</sup>*Accelerator Laboratory, Department of Physics, University of Helsinki, P.O. Box 43, FI-00014 Helsinki, Finland*

*\*Also at: Institute of Physics, University of Tartu, W. Ostwald 1, 50411 Tartu, Estonia, e-mails:kaupo.kukli@helsinki.fi, kaupo.kukli@ut.ee*

## Abstract

Amorphous SiO<sub>2</sub>-Nb<sub>2</sub>O<sub>5</sub> nanolaminates and mixture films were grown by atomic layer deposition. The films were grown at 300 °C from Nb(OC<sub>2</sub>H<sub>5</sub>)<sub>5</sub>, Si<sub>2</sub>(NHC<sub>2</sub>H<sub>5</sub>)<sub>6</sub>, and O<sub>3</sub> to thicknesses ranging from 13 to 130 nm. The niobium to silicon atomic ratio was varied in the range of 0.11-7.20. After optimizing the composition, resistive switching properties could be observed in the form of characteristic current-voltage behavior. Switching parameters in the conventional regime were well defined only in a SiO<sub>2</sub>:Nb<sub>2</sub>O<sub>5</sub> mixture at certain, optimized, composition with Nb:Si atomic ratio of 0.13, whereas low-reading voltage measurements allowed recording memory effects in a wider composition range.

**Keywords:** atomic layer deposition, niobium oxide, silicon oxide, nanolaminates, multilayers, resistive switching, memory

## Introduction

Artificially mixed or layered nanomaterials, particularly those consisting of different oxides, have been of continuously growing interest due to the possibility to tailor functional properties of the constituent compounds, thus extending their application areas. Regarding one of the most basic materials, silicon oxide, one can note that thin solid films containing SiO<sub>2</sub> have been grown and investigated for several purposes, including porous membranes [1], catalysts [2,3], and optical filters [4,5]. SiO<sub>2</sub> films, mixtures of SiO<sub>2</sub> with metal oxides, and other SiO<sub>2</sub>-based nanostructures have been synthesized by different methods such as

galvanostatic etching of SiO<sub>2</sub> [6], electron beam evaporation [4,7, 8], sputtering [5,9-17], sol-gel technique [2], chemical vapor deposition [17], and atomic layer deposition (ALD). In the latter case, growth of silicon oxide could effectively be realised using, e.g, tris(dimethylamino)silane [1] or hexakis(ethylamino)disilane [18-19] as silicon precursors and ozone.

SiO<sub>2</sub>-Nb<sub>2</sub>O<sub>5</sub> multilayers have been investigated as optical coatings [8-11]. Multilayering Nb<sub>2</sub>O<sub>5</sub> with SiO<sub>2</sub> films has allowed one to reduce internal mechanical stress in the optical coating [10] and, of course, tailor the refractive index and reflecting properties of the coatings [8-9]. Nb<sub>2</sub>O<sub>5</sub> itself as a dielectric high permittivity metal oxide has been considered for the application in dynamic random access memories [20,21], also when tailored with Ta<sub>2</sub>O<sub>5</sub> or Al<sub>2</sub>O<sub>3</sub> [22-24].

In certain aspects, nanolaminates as switching media might demonstrate improved performance due to their stacked or periodical structure which can, at first, limit excessive grain growth. Secondly, the internal interfaces in multilayers can confine rupture points of conduction paths or filaments and, thirdly, internal barriers built in the laminates can suppress oxygen ion transport.

A polycrystalline material layer with random distribution of crystallite boundaries may give rise to nonuniformity or instability of resistive switching parameters such as ratios between the high and low resistance states as well as variability in switching (programming) voltages. These instabilities would thereby be consequences of the variations in the size, direction, and length of the conduction paths, especially in the case of filamentary conduction. In order to improve the reliability, one can deposit alternate layers of lower and higher electrical resistance materials. Such kind of structural tuning has been applied, e.g., in Al<sub>2</sub>O<sub>3</sub>/HfO<sub>2</sub>/Al<sub>2</sub>O<sub>3</sub> stacks where, as proposed, the tips of localized conduction paths led to the formation or rupture of the conducting filaments mainly at the interfaces between HfO<sub>2</sub> and Al<sub>2</sub>O<sub>3</sub> layers during the SET and RESET events [25]. The same concept was proposed to suppress the endurance fluctuation by controlling the filament rupture points to internal interfaces in double-layered media consisting of HfO<sub>2</sub> and ZrO<sub>2</sub> layers [26]. Yet in another study, the suppression of data retention failures, i.e. reliability increment, was directly attributed to the blocking of oxygen ion transport by an Al<sub>2</sub>O<sub>3</sub> layer in HfO<sub>2</sub>/Al<sub>2</sub>O<sub>3</sub>

multilayers [27]. Increased control over lengths and depths of the switchable conduction paths enabled stabilization of the switching parameters and increase in the reliability of the memristive characteristics.

As was stated earlier [28], interfaces between the component layers in laminates allow one to control the electronic band structure of the system leading to the barriers for charge transport, introduce local mechanical strains influencing structure and crystallization at the interface, and thus provide additional degrees of freedom for device implementation. In a comparative study on  $\text{Al}_2\text{O}_3$  and  $\text{HfO}_2$  single layers, and  $\text{Al}_2\text{O}_3/\text{HfO}_2$  nanolaminates [29], the superiority of the nanolaminates over single layers in terms of uniformity and self-compliance was demonstrated.

Stacks and periodical nanolaminates for ReRAM cells can be fabricated by physical vapor deposition, using, e.g., sputtering technique [26,30]. Hereby atomic layer deposition method has become the emerging method for the fabrication of switching media consisting of, e.g.,  $\text{Al}_2\text{O}_3$  and  $\text{HfO}_2$  [25,27,28], or  $\text{Al}_2\text{O}_3$  and  $\text{TiO}_2$  [28].

$\text{Ta}_2\text{O}_5$  has probably been the most extensively considered and prospective memristor oxide [31], whereas  $\text{Nb}_2\text{O}_5$  films have been studied less frequently for this purpose, although  $\text{Nb}_2\text{O}_5$  is related to  $\text{Ta}_2\text{O}_5$  in terms of abundance, crystallography, electronic and optical properties.  $\text{Nb}_2\text{O}_5$  may be regarded as somewhat more conductive (electrically leaky) oxide compared to  $\text{Ta}_2\text{O}_5$ , due to its smaller band gap [23, 32], and possibly larger stoichiometry deviations accompanied by oxygen vacancies. Despite the electrically relatively leaky character of niobium oxide, memristive structures [33] based on  $\text{Nb}_2\text{O}_5$  have been proposed, either combined with  $\text{Ta}_2\text{O}_5$  [34], deposited as single oxide layers [33-38], or layered alternately with other oxides such as  $\text{TiO}_2$  [39]. The effective band gap of  $\text{Nb}_2\text{O}_5$  can be widened and, concurrently, insulating properties improved in  $\text{Nb}_2\text{O}_5$  films upon mixing them with wider-band-gap oxides such as  $\text{Al}_2\text{O}_3$  [40] or  $\text{SiO}_2$ . Electronic properties of wider band-gap  $\text{Al}_2\text{O}_3$  doped with  $\text{Nb}_2\text{O}_5$  by ALD using  $\text{Nb}(\text{OC}_2\text{H}_5)_5$  and water as precursors have been investigated [41]. Regarding the ALD method,  $\text{Nb}_2\text{O}_5$  films have mainly been grown from  $\text{Nb}(\text{OC}_2\text{H}_5)_5$  and water [42, 43]. ALD- $\text{Nb}_2\text{O}_5$  has been studied as a component of negative electrode in energy storage microdevices [44], or as a resistively switching medium [45].

SiO<sub>2</sub> has also been considered as a prospective memristive material exhibiting resistive switching behavior either deposited alone [12,46,47] or combined with metals or metal oxides [7,13-17]. Many metal oxides have, to date, been explored and listed as candidates for memristive dielectrics [48] but SiO<sub>2</sub> has been described as a compound which after combination with some other oxides or metals may actually promote the resistive switching behavior in a hosting metal oxide [49].

In the present paper, ALD of SiO<sub>2</sub>-Nb<sub>2</sub>O<sub>5</sub> mixture films and nanolaminates was carried out using a novel combination of cation precursors: niobium pentaethoxide, Nb(OC<sub>2</sub>H<sub>5</sub>)<sub>5</sub>, and hexakis(ethylamino) disilane, Si<sub>2</sub>(NHC<sub>2</sub>H<sub>5</sub>)<sub>6</sub>. Ozone, O<sub>3</sub>, was applied as an oxidizer. The goal of the study was to obtain primary knowledge about the correlation between elemental composition, cation ratio, and growth cycle ratio of the constituent oxides. In terms of functionality, the Nb<sub>2</sub>O<sub>5</sub>-SiO<sub>2</sub> films were characterized by electrical measurements conducted in the resistive switching regime. The goal of the electrical evaluation was to clarify whether the multilayers grown at a rather low temperature (300 °C) and stacked between electrodes of moderate work function could perform as switching media. It was examined whether it is possible to empirically find a balance between defect densities and composition of the mixtures in order to improve their electrical performance. Further, small signal current and admittance measurement procedures were exploited to help distinction of the conductance states also in the case of films which are so leaky that the low and high resistivity states become difficult to distinguish in the common d.c. measurements.

## Experimental details

The films were grown in a commercial flow-type hot-wall reactor F120 [50] (ASM Microchemistry, Ltd.). Growth temperature was held at 300 °C. The silicon precursor used was hexakis(ethylamino)disilane [18,19], i.e. Si<sub>2</sub>(NH<sub>2</sub>Et)<sub>6</sub>, AHEAD (Air Liquide, Inc.), evaporated at 65-67 °C. The niobium precursor, Nb(OC<sub>2</sub>H<sub>5</sub>)<sub>5</sub>, was evaporated at 90-93 °C. Both precursors were evaporated from open boats inside the reactor, and transported to the substrates by the N<sub>2</sub> flow. The pressure in the reactor chamber during the deposition process was below 10 mbar. Ozone as the oxygen precursor was produced with a Wedeco Ozomatic

Modular 4 HC ozone generator from oxygen (99.999%, Linde Gas). The estimated ozone concentration output of the generator was about 100 g/m<sup>3</sup>.

The cycle times used were 0.5-0.5-2.0-0.5 s, denoting the sequence Si or Nb precursor pulse–purge–O<sub>3</sub> pulse–purge. The substrates were pieces of wafers, cut out of undoped Si(100) covered with less than 2.0 nm thick wet-chemically-grown SiO<sub>2</sub>. Electrically conducting substrates were also used, based on (100) silicon with a resistivity of 0.014–0.020 Ω · cm, i.e., Si boron-doped to the concentrations up to  $5 \times 10^{18} - 1 \times 10^{19}/\text{cm}^3$ , and coated with 10 nm thick titanium nitride layer. Such structures enable convenient through-wafer measurements during electrical evaluation of the oxide layers. TiN was chemical vapor deposited using TiCl<sub>4</sub>/NH<sub>3</sub> process in an ASM A412 Large Batch 300 mm reactor at Fraunhofer IPMS-CNT. The SiO<sub>2</sub>-Nb<sub>2</sub>O<sub>5</sub> films were grown to thicknesses ranging from ca. 10 to 150 nm. The thickest films were grown for the convenience of composition analysis.

X-ray diffraction (XRD) measurements were performed with PANalytical X'Pert Pro MPD diffractometer using CuK $\alpha$  radiation (1.5406 Å), 1/4° divergence slit and parallel beam optics. The same setup with a smaller 1/16° divergence slit, Cu attenuator and parallel plate collimator slit was used for X-ray reflectivity (XRR) measurements. The density, thickness and roughness of the layers was acquired by fitting the theoretical model to the measured data using either Reflectivity 1.2 (PANalytical) or Reflex35 [51] softwares. Energy dispersive X-ray spectrometry (EDX) was used for the measurements of the relative niobium and silicon contents in the films by a Hitachi S-4800 scanning electron microscope (SEM) equipped with an Oxford INCA 350 EDX spectrometer. In order to avoid interference from the substrate while measuring the silicon content, these measurements were done on samples grown on aluminum foil placed into the reactor chamber simultaneously with the samples grown on silicon. The EDX spectra were measured at 10 keV. The beam current and spectrometer gain were determined from a calibration measurement performed under the same beam conditions. The calculations were done on the basis of k ratios measured for Nb L $\alpha$  and Si K $\alpha$  X-ray lines using a GMRFILM program [52]. Oxygen was calculated from the stoichiometry. The error of the EDX measurements was ~10 %, and could increase to 15 % in the case of the thinnest films, e.g. the 13 nm thick reference Nb<sub>2</sub>O<sub>5</sub>. Contents of residual light elements in selected representative samples were determined by time-of-flight elastic recoil detection

analysis (TOF-ERDA) [53]. The TOF-ERDA was performed with 5 MV tandem accelerator using 50 MeV  $^{127}\text{I}$  ion beam.

In order to carry out the electrical measurements, metal-insulator-metal (MIM) structures were prepared on the conducting substrates where the TiN served as the bottom electrode. Top electrodes with an area of either 0.052 or 0.204 mm<sup>2</sup> were formed by electron beam evaporation of 120 nm thick Al/Ti dot electrodes through a shadow mask, with the Ti layer contacting the SiO<sub>2</sub>-Nb<sub>2</sub>O<sub>5</sub> dielectric layers. Admittance-voltage and current-voltage measurements were carried out in a light-proof and electrically shielded box. Samples were electrically characterized in both d.c. and a.c. regimes using a Keithley 4200SCS semiconductor analyzer. The bias voltage was applied to the top electrode, while the bottom electrode was grounded. To record the admittance parameters, a small signal of 30 mV r.m.s. was superimposed with the d.c. bias voltage. The measurement frequency did not affect the resistive switching behavior in the range of 20 kHz - 1 MHz.

## Results and discussion

The Nb to Si ratio was varied by changing the ratio of the SiO<sub>2</sub> and Nb<sub>2</sub>O<sub>5</sub> deposition cycles. The numbers of these deposition cycles were varied separately in order to change the thicknesses of the constituent metal oxide layers. In this way, films of different artificial structures were deposited, ranging from SiO<sub>2</sub> doped or mixed with low amounts of Nb<sub>2</sub>O<sub>5</sub> to SiO<sub>2</sub>-Nb<sub>2</sub>O<sub>5</sub> nanolaminates. The growth cycle sequences applied for the different samples are presented in [Table I](#).

ToF-ERDA results of selected films are depicted in [Figures 1](#) and [2](#) in the form of elemental depth profiles. ToF-ERDA was conducted in order to examine the chemical purity of the films especially in terms of the light residual elements, hydrogen and carbon, originating primarily from the precursor ligands. Elemental contents were calculated omitting the very surface as well as the substrate-film interface.

**Table I.** ALD cycle sequences for SiO<sub>2</sub>-Nb<sub>2</sub>O<sub>5</sub> films with the thicknesses and Nb:Si cation ratios measured by EDX in the order of ascending Nb/Si ratio.

Cycle sequence	notes	Nb:Si EDX at. ratio	EDX thickness, nm
2000 × SiO <sub>2</sub>	thick reference SiO <sub>2</sub>	0	122
250 × SiO <sub>2</sub>	reference SiO <sub>2</sub>	0	18
20 × [ 10 × SiO <sub>2</sub> + 2 × Nb <sub>2</sub> O <sub>5</sub> ] + 10 × SiO <sub>2</sub>	Nb <sub>2</sub> O <sub>5</sub> -doped SiO <sub>2</sub>	0.11	19
50 × [ 5 × SiO <sub>2</sub> + 1 × Nb <sub>2</sub> O <sub>5</sub> ] + 5 × SiO <sub>2</sub>	Nb <sub>2</sub> O <sub>5</sub> -doped SiO <sub>2</sub>	0.13	22
10 × [ 50 × Nb <sub>2</sub> O <sub>5</sub> + 150 × SiO <sub>2</sub> ] + 50 × Nb <sub>2</sub> O <sub>5</sub>	thick laminate with thicker SiO <sub>x</sub>	0.18	ca. 110
350 × [ 3 × Nb <sub>2</sub> O <sub>5</sub> + 3 × SiO <sub>2</sub> ] + 3 × Nb <sub>2</sub> O <sub>5</sub>	thick mixture	0.40	133
150 × [ 1 × Nb <sub>2</sub> O <sub>5</sub> + 1 × SiO <sub>2</sub> ] + 1 × Nb <sub>2</sub> O <sub>5</sub>	thin „homogeneous“ mixture	0.46	19
1000 × [ 1 × Nb <sub>2</sub> O <sub>5</sub> + 1 × SiO <sub>2</sub> ] + 1 × Nb <sub>2</sub> O <sub>5</sub>	thick „homogeneous“ mixture	0.48	120
30 × [ 12 × Nb <sub>2</sub> O <sub>5</sub> + 3 × SiO <sub>2</sub> ] + 12 × Nb <sub>2</sub> O <sub>5</sub>	SiO <sub>2</sub> -doped Nb <sub>2</sub> O <sub>5</sub>	1.2	19
5 × [ 55 × Nb <sub>2</sub> O <sub>5</sub> + 15 × SiO <sub>2</sub> ] + 55 × Nb <sub>2</sub> O <sub>5</sub>	thin „defined“ laminate	1.6	18
15 × [ 30 × Nb <sub>2</sub> O <sub>5</sub> + 2 × SiO <sub>2</sub> ] + 30 × Nb <sub>2</sub> O <sub>5</sub>	SiO <sub>2</sub> -doped Nb <sub>2</sub> O <sub>5</sub>	2.9	21
10 × [ 170 × Nb <sub>2</sub> O <sub>5</sub> + 20 × SiO <sub>2</sub> ] + 170 × Nb <sub>2</sub> O <sub>5</sub>	thick laminate, „thick“ NbO <sub>x</sub>	3.5	78
30 × [ 15 × Nb <sub>2</sub> O <sub>5</sub> + 1 × SiO <sub>2</sub> ] + 15 × Nb <sub>2</sub> O <sub>5</sub>	SiO <sub>2</sub> -doped Nb <sub>2</sub> O <sub>5</sub>	7.2	19
350 × Nb <sub>2</sub> O <sub>5</sub>	reference Nb <sub>2</sub> O <sub>5</sub>	-	13

The SiO<sub>2</sub> film grown on Si(100) substrate using 2000 ALD cycles (Fig. 1) contained 28.2 ± 0.3 at.% silicon, 64.0 ± 0.5 at.% oxygen, 7.7 ± 0.6 at.% hydrogen, less than 0.01 at.% carbon, and less than 0.03 at.% nitrogen. The SiO<sub>2</sub>-Nb<sub>2</sub>O<sub>5</sub> film grown using the cycle sequence 1000 × [ 1 × Nb<sub>2</sub>O<sub>5</sub> + 1 × SiO<sub>2</sub> ] + 1 × Nb<sub>2</sub>O<sub>5</sub> (Fig. 2) contained 21.0 ± 0.3 at.% silicon, 8.9 ± 0.1 at.% niobium, 68.3 ± 0.5 at.% oxygen, 1.5 ± 0.3 at.% hydrogen, 0.23 ± 0.03 at.% carbon, and 0.15 ± 0.02 at.% nitrogen. The Nb:Si cation ratio measured for the latter film by EDX on Al foil was 0.48, compared to the ratio of 0.42 obtained by ToF-ERDA. Thus the EDX and ToF-ERDA results agree reasonably well in terms of film composition.

It can be seen, that the hydrogen content is markedly high in the SiO<sub>2</sub> films (Figure 1), exceeding 7 at.%. At the same time, in the films mixed with Nb<sub>2</sub>O<sub>5</sub> (Figure 2) the hydrogen content was decreased down to 1-2 at.%. In addition, elemental composition of a 15 nm thick reference Nb<sub>2</sub>O<sub>5</sub> film was measured. The elements were detected in the relative contents of 27 ± 0.5, 71.2 ± 1.4 and 0.91 ± 0.13 at. % for niobium, oxygen and hydrogen, respectively. The

content of carbon remained below the reliable measurement level in this  $\text{Nb}_2\text{O}_5$  sample, i.e. below 0.2 at.%. No other elements were detected.

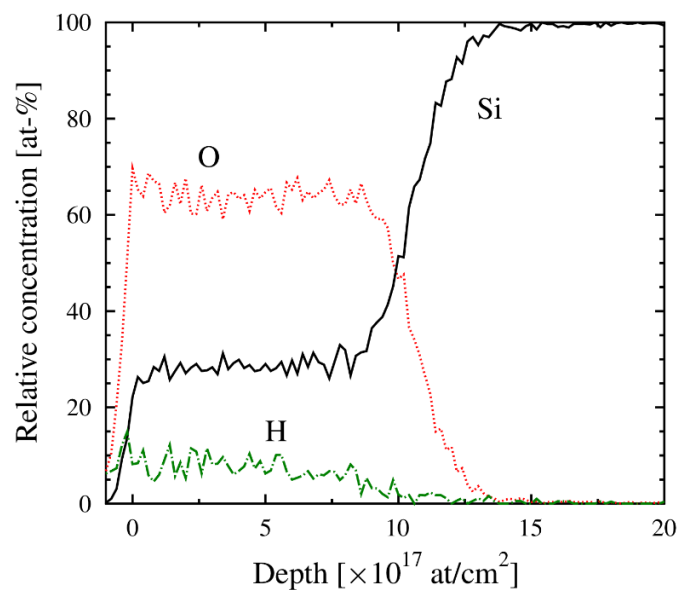


**Figure 1.** Elemental depth profile from ToF-ERDA for a  $\text{SiO}_2$  film grown on  $\text{Si}(100)$  substrate using 2000 ALD cycles. The thickness measured by EDX was 122 nm.

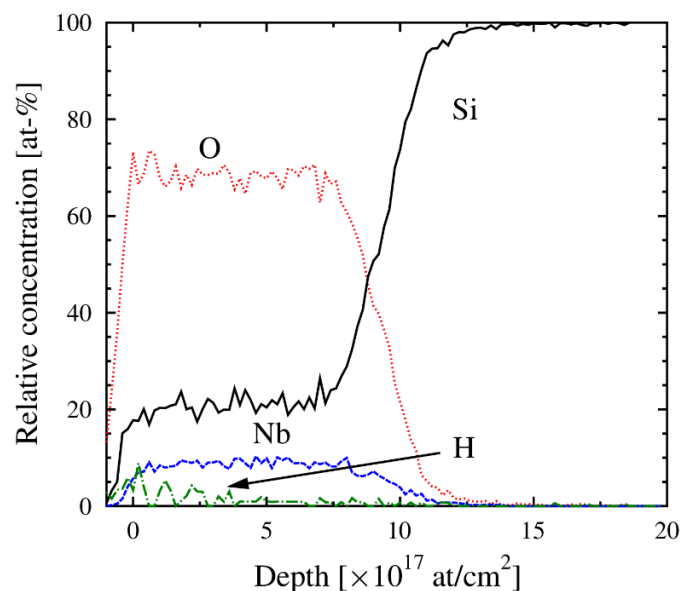


**Figure 2.** Elemental depth profile from ToF-ERDA for a  $\text{Nb}_2\text{O}_5\text{-SiO}_2$  film grown on  $\text{Si}(100)$  substrate using cycle sequence of  $1000 \times [1 \times \text{Nb}_2\text{O}_5 + 1 \times \text{SiO}_2] + 1 \times \text{Nb}_2\text{O}_5$ . The thickness measured by EDX was 120 nm.



All the films - single oxides, mixed oxides and nanolaminates - were amorphous as examined by X-ray diffraction measurements. X-ray reflectivity (XRR) measurements were performed to examine the distinction between the  $\text{SiO}_2$  and  $\text{Nb}_2\text{O}_5$  layers constituting the nanolaminate. In this way, one could prove the nanolaminate structure of the samples with relatively thicker constituent metal oxide layers. XRR measurements of selected samples showed a clear evidence of layered structure consisting of the niobium and silicon oxides (Fig. 3). The highest sharp maxima that are the most prominent, are characteristic of the superlattice structures [54-57] and indicate that the bilayers are uniform with appreciably sharp interfaces. The period of the superlattice maxima becomes gradually longer or shorter as the bilayer thickness decreases or increases, respectively [54-57]. The shorter oscillation period is inversely proportional to the total nanolaminate thickness. These shorter oscillations are in a good agreement with the simulations, giving further evidence of an appreciable layer thickness uniformity (Fig. 3). Anyhow, some variations in the intermediate layer thicknesses and densities may be caused by thickness profiles formed across the substrate due to the deviations in adsorption rates and nucleation densities along the gas flow directions in the cross-flow type reactor used. The niobium oxide layers deposited with smaller numbers of cycles have lower densities, which is quite natural because these films represent the earliest stages of the nucleation and growth (Fig. 3). Such factors may also somewhat complicate the modelling of relatively complex reflection patterns obtained from the periodical multilayers.

Further proof of the nanolaminate quality was obtained by fitting the measured data, as the stack could be modelled adequately by repeating equal bilayers of  $\text{Nb}_2\text{O}_5$  and  $\text{SiO}_2$  and a  $\text{Nb}_2\text{O}_5$  capping layer on top. In other words, all the bilayers in the nanolaminate were considered equal. The differences observed in the Figure 3, the top and second panels in the left column, are due to small differences between the adjacent bilayers. Thus, the nanolaminates, which were deposited using the different cycle sequences indicated in the Table I and in Fig. 3 allowed one to achieve satisfactory fit between the measured data and modelled curves. Native  $\text{SiO}_2$  layer of ~1.2-1.4 nm thickness had to be included between the film and silicon substrates in the models in order to achieve the best fits.

As mentioned above, the period of the maxima caused by the multilayer structure considerably increased due to the decrease in the bilayer thickness. Obviously, in order to visualise the ordering in the multilayer with the thinnest interlayers in this study, one had to measure the reflectivity patterns in markedly extended ranges of angles (Fig. 3). It became evident, that two ALD cycles of SiO<sub>2</sub> deposited alternately with the hosting Nb<sub>2</sub>O<sub>5</sub> layers was sufficient to create multilayered structures with distinctive periodicity. Thus, the film deposited using the cycle sequence  $15 \times [30 \times \text{Nb}_2\text{O}_5 + 2 \times \text{SiO}_2] + 30 \times \text{Nb}_2\text{O}_5$  (Fig. 3, the 3rd panel), was modelled to consist of 1.05 nm thick Nb<sub>2</sub>O<sub>5</sub> and, nominally, 0.07 nm thick SiO<sub>2</sub> layers, providing a satisfactory fit with the measured curve. The thickness obtained for SiO<sub>2</sub>, 0.07 nm, remains below a thickness of a monolayer, meaning that the SiO<sub>2</sub> layer was not continuous, and the result rather reflects a periodical two-dimensional confinement of the elemental constituents with specific electron density, within the multilayer structure.

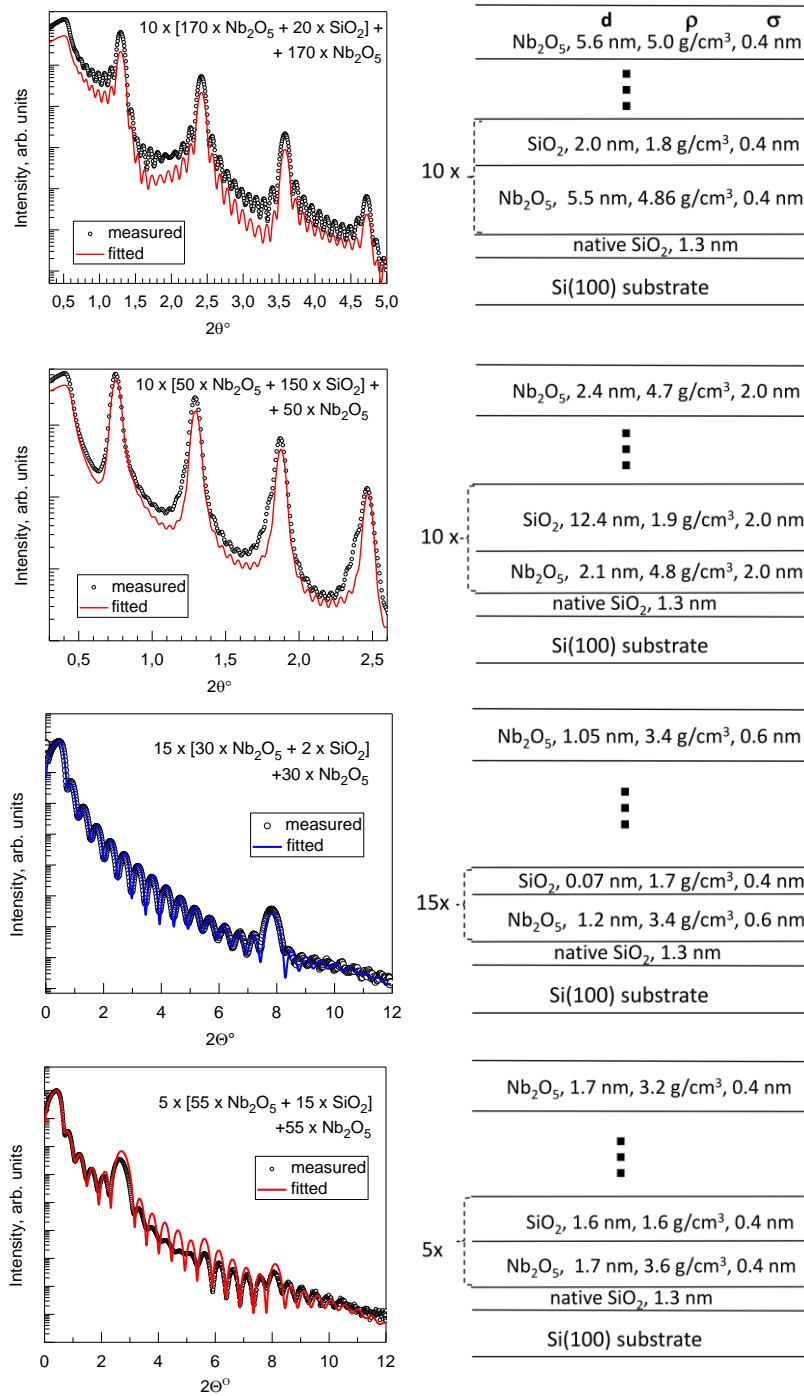


**Figure 3.** Representative X-ray reflectivity patterns measured from  $\text{Nb}_2\text{O}_5$ - $\text{SiO}_2$  nanolaminates deposited using ALD cycle sequences as given by labels, and thickness,  $d$ , density,  $\rho$ , and roughness,  $\sigma$  (right column), as results obtained from fitting the XRR patterns. Note the differences in the ranges of the measurement angles. In the two upper panels of the left column, the measured and fitted curves are shifted vertically in relation to each other for the sake of clarity. The schematic layer thicknesses in the right column are not to scale.

## Electrical performance

Leakage currents in Nb<sub>2</sub>O<sub>5</sub> and SiO<sub>2</sub>-Nb<sub>2</sub>O<sub>5</sub> nanolaminates occurred too high for the reliable recognition and stabilization of low resistivity state when measured in the RRAM regime. In such samples, no current-voltage hysteresis and memory windows between low resistance states (LRS) and high resistance states (HRS) developed. Besides the highly defective nature of amorphous Nb<sub>2</sub>O<sub>5</sub> films and their likely oxygen deficiency, high leakage current could also arise due to the application of low work function Ti and TiN electrodes. Earlier, resistive switching behavior of Nb<sub>2</sub>O<sub>5</sub> grown by ALD from Nb(OC<sub>2</sub>H<sub>5</sub>)<sub>5</sub> and water has been recognized when the Nb<sub>2</sub>O<sub>5</sub> films were stacked between higher work function and noble platinum bottom and top Ti electrodes [45]. In the present study, the emphasis was put on the behavior of the dielectric material and its internal ability or disability to host the switching current. As a result and in a clear contrast with the nanolaminates, behavior characteristic of RRAM material was achieved and recorded with the SiO<sub>2</sub>-Nb<sub>2</sub>O<sub>5</sub> mixture films grown using SiO<sub>2</sub>:Nb<sub>2</sub>O<sub>5</sub> ALD cycle ratio of 5:1 (Figure 4, top panel).

Figure 4, middle panel, depicts in a generalized form the voltage and corresponding current signals applied and measured, respectively, on resistively switching stacks consisting of an oxide or a combination of different oxides, mounted between metallic electrodes. During the conventional resistive switching measurement, rectangular voltage pulses are applied on the electrodes, with the amplitude increasing within the sequence of pulses. At the increasing voltage pulses, values of current are recorded, which, in the sequence, form the current-voltage curve until the transition (switching) to the low resistance state. Upon back-forth sweeping the sequence of voltage pulses with gradually and alternately increasing and decreasing amplitudes, the envelope curves of the current-voltage dependences were recorded (Fig. 4, top panel) with hysteresis characteristic of resistive switching behavior in a memristive material. Fig. 4 thus depicts defined memristive behavior characterizing Nb<sub>2</sub>O<sub>5</sub>:SiO<sub>2</sub> films with Nb:Si atomic ratio of 0.13 grown using SiO<sub>2</sub>:Nb<sub>2</sub>O<sub>5</sub> cycle ratio of 5:1.

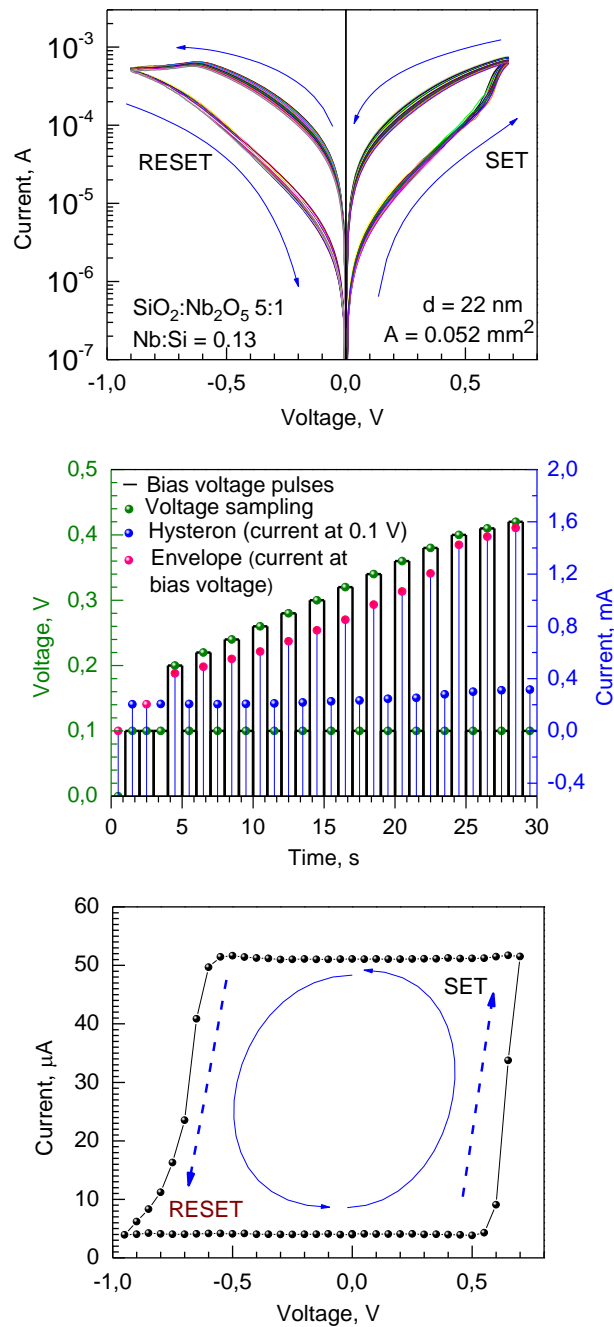


**Figure 4** Sequential current-voltage loops measured in resistive switching regime from 22 nm thick  $\text{SiO}_2\text{-Nb}_2\text{O}_5$  film deposited with  $\text{SiO}_2:\text{Nb}_2\text{O}_5$  cycle ratio of 5:1 (upper panel); sampling voltage pulses applied on a film to record switching currents and small signal current values detected at 0.1 V as memory maps (middle panel); and current-voltage loop measured at low-reading voltage (0.1 V) (bottom panel).

Besides the envelope curves consisting of current values measured at the variable bias voltage amplitudes, low reading voltage hysteron curves were recorded as well. In the latter case, currents were read at voltage values of 0.1 V in between the sequential sampling bias voltage pulses. The value of the measured current was, dominantly, determined by the two resistivity states achieved alternately, and two clearly defined plateaus were reached and passed through before and after the sequential SET and RESET transitions (Fig. 4, bottom panel). Current-voltage loop with remarkable squareness, also defined as a current memory map, was thus formed with the memory window between the high and low current states reaching 0.023 A/cm<sup>2</sup>.

Admittance parameters were also recorded while sweeping the bias voltage. In order to measure differential capacitance, 30 mV rms ac signal at a frequency of 500 kHz was superimposed to the voltage bias. Parallel admittance model [58] was exploited to determine conductance, G, and capacitance, C, values against lowreading voltage sampling. In order to obtain the memory maps for G and C return-to-zero voltage pulse sequences were used. That is, on the sample in high resistance state, positive voltage pulses of 1 ms were applied. After each pulse, the voltage was returned to 0 V and the admittance-derived values (G, C) were recorded immediately. The amplitude of the voltage pulse ( $V_P$ ) was increased linearly until the transition from the high resistance state to the low resistance state occurred. Once the sample had reached the low resistance state,  $V_P$  was linearly decreased in the opposite direction, i.e. towards negative values. When the  $V_P$  reached values negative enough to enable switching the device back to the high resistance state (i.e. provide RESET transition), it was linearly increased to the zero voltage. The plots of C (Fig. 5) and G (Fig. 6) as functions of the bias voltage,  $V_P$ , thus constituted the corresponding memory maps. The bias sampling voltage herewith serves also as the programming voltage.

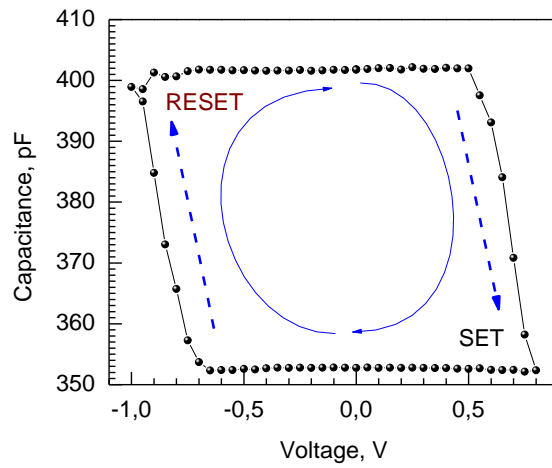


**Figure 5.** Capacitance-voltage hysteron loop measured at programming voltage values during sampling voltage pulse swept on 22 nm thick  $\text{SiO}_2\text{-Nb}_2\text{O}_5$  film deposited with  $\text{SiO}_2\text{:Nb}_2\text{O}_5$  cycle ratio of 5:1.

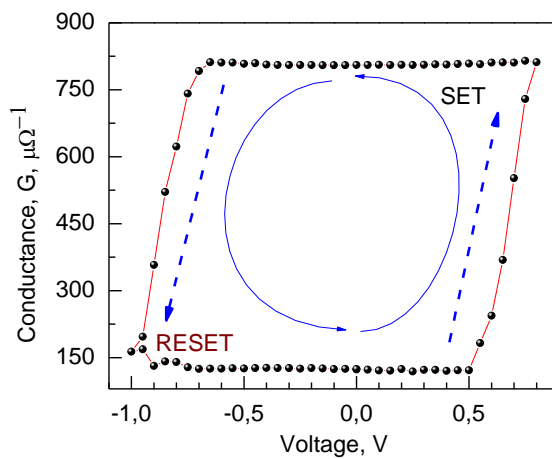


**Figure 6.** Conductance-voltage hysteron loop measured at programming voltage values during sampling voltage pulse swept on 22 nm thick  $\text{SiO}_2\text{-Nb}_2\text{O}_5$  film deposited with  $\text{SiO}_2\text{:Nb}_2\text{O}_5$  cycle ratio of 5:1.

The parameters of the memory maps, i.e., the switching voltages (fields), and windows between conductance and capacitance extrema, were rather insensitive to the measurement frequency in the whole range examined, 20 kHz – 1 MHz. Regardless of frequency,  $G_0$  and  $C_0$  remained very stable in a wide  $V_P$  range, being indicative of stable conduction paths formed during switching. The width of the conductance hysteron extended to  $700 \mu\Omega^{-1}$ , with 110 and  $800 \mu\Omega^{-1}$  in high and low resistivity states, respectively, promising lowered power consumption while storing information if read at the high resistivity state. RESET and SET transitions were well-defined one-step processes (Figs. 5, and 6), although not as abrupt as RESET in the case of some other materials, such as Ta<sub>2</sub>O<sub>5</sub>-TiO<sub>2</sub>-Ta<sub>2</sub>O<sub>5</sub> trilayer structures also grown by ALD [58]. In the latter case, the SET process tended to be gradual, passing certain steps between the high and low resistance states, which is not observed in the present case. It is possible, that a few-layer stacks may become more asymmetric being RESET more steeply than SET with an implication that switching on, as well as restoring highly conductive state can be an instantaneous process, whereas its breaking and disappearance is more gradual. For instance, in the present case, in a 22 nm thick film grown using cycle sequence of  $50 \times [5 \times \text{SiO}_2 + 1 \times \text{Nb}_2\text{O}_5] + 5 \times \text{SiO}_2$ , both SET and RESET transitions could become relatively slow without marked dependence on polarity. Earlier, certain differences in conduction current densities in materials between Ti and TiN contact electrodes were measured [60] and, assumptionally, asymmetric behavior of oxide stacks between Ti and TiN could be assumed. Nonetheless, the resistive switching performance in the case of SiO<sub>2</sub>:Nb<sub>2</sub>O<sub>5</sub> film with thin SiO<sub>2</sub>:Nb<sub>2</sub>O<sub>5</sub> intermediates grown using small numbers of the growth cycles for both constituents in periodical stacks remained symmetric. The latter was valid at least when the film had appreciably high thickness. Further, a more important issue related to the possibility of application of such material layers, was generally connected to the highly leaky nature of SiO<sub>2</sub>:Nb<sub>2</sub>O<sub>5</sub> films, accompanied by difficulties in keeping the material initially in a low resistivity state, and also difficulties to find the appropriate cycle and cation ratios between the constituent oxides to provide switching resistance regime.

In the rest of the films grown in this study, the leakage currents occurred too high for the clear distinction between the low and high resistance states in the conventional resistive switching regime. The memory window between the currents in LRS and HRS remained inadequately narrow for reliable resistive switching behavior (Fig. 7, topmost panel). That was most likely due to the leaky nature of both Nb<sub>2</sub>O<sub>5</sub> and SiO<sub>2</sub> layers, at first due to their disordered structure



and, secondly, also because of the relatively high contents of residual elements, such as hydrogen. In the nanolaminate structures, the potential barriers likely forming between the constituent oxide layers may, in some extent, assist in suppressing leakage currents. However, in the present case the number of barriers, if existing in such thin films, were clearly not high enough to compensate the detrimental effects of structural and chemical disorder.

It is noteworthy that the small signal current hysteron measurements enabled significantly improved distinction between the two resistivity states in the film grown with a  $\text{SiO}_2\text{:Nb}_2\text{O}_5$  cycle ratio of 10:2 (Fig. 7, the 2nd panel from top). The current-voltage loops within the low-voltage measurements were, obviously, not as well defined in terms of squareness as those in the adequately performing  $\text{SiO}_2\text{-Nb}_2\text{O}_5$  sample grown with a cycle ratio of 5:1 (Fig. 4, bottom panel). However, the measurement mode had a major effect in terms of the distinction between the memory states. Notably, that behavior was recorded for capacitance (Fig. 7, the 3rd panel from top) and conductance (Fig. 7, bottom panel) as well.

Similar results were found for other selected samples as well as for reference  $\text{SiO}_2$  film (not shown), which alone could not satisfactorily perform as memristive material, plausibly due to high amount of residues, such as hydrogen, and also carbon. Clearly, to ensure performance of materials as resistively switching media, one has to either adjust the composition of mixtures at high accuracy, or write/read the resistivity states in the admittance regime.

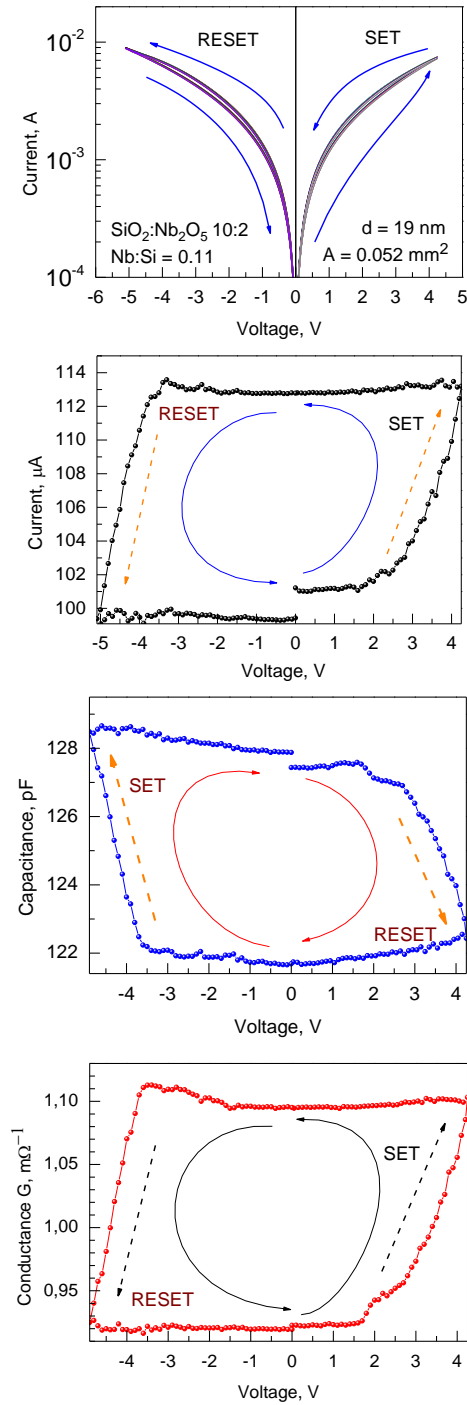


**Figure 7.** Current-voltage loops measured in conventional resistive switching mode (top panel); low-reading voltage memory map (the 2nd panel from top), small signal capacitance memory map (the 3rd panel from top); and small signal conductance memory map (bottom panel) against sampling voltage pulses applied on 19 nm thick  $\text{SiO}_2\text{-Nb}_2\text{O}_5$  film deposited with  $\text{SiO}_2:\text{Nb}_2\text{O}_5$  cycle ratio of 10:2.

## Conclusions

Thin mixed films and nanolaminates consisting of Nb<sub>2</sub>O<sub>5</sub> and SiO<sub>2</sub> layers grown alternately by atomic layer deposition were devised at a substrate temperature of 300 °C. The precursor system used was a novel combination of Nb(OC<sub>2</sub>H<sub>5</sub>)<sub>5</sub>, Si<sub>2</sub>(NHC<sub>2</sub>H<sub>5</sub>)<sub>6</sub>, and O<sub>3</sub>. The niobium to silicon atomic ratio in the films grown to thicknesses from 13 to 130 nm was varied in the range of 0.11-7.20. The films were amorphous in the as-deposited state and were also characterized in the as-deposited state.

In the nanolaminate structures consisting of 2-5 nm thick distinct layers, the densities of Nb<sub>2</sub>O<sub>5</sub> and SiO<sub>2</sub> layers reached 4.9 and 1.8 g/cm<sup>3</sup>, respectively, approaching bulk values. The content of hydrogen as the main light residue exceeded 7 at. % in SiO<sub>2</sub>, but decreased in mixed SiO<sub>2</sub>-Nb<sub>2</sub>O<sub>5</sub> films down to 1-2 at.%, and in reference Nb<sub>2</sub>O<sub>5</sub> film even below the reliable measurement level.

Electrical measurements on Nb<sub>2</sub>O<sub>5</sub>-SiO<sub>2</sub> nanolaminates implied that the performance of the films was strongly influenced by the relative content of the constituent oxides in the whole structure. Appreciably high current ratios between the high and low resistance states extending over two orders of magnitude could actually be achieved only in a mixture film deposited with a SiO<sub>2</sub>:Nb<sub>2</sub>O<sub>5</sub> cycle ratio of 5:1, possessing Nb:Si cation ratio of 0.13. At the same time, small signal measurements enabled recording, in several SiO<sub>2</sub> and Nb<sub>2</sub>O<sub>5</sub> based films, voltage-dependent admittance maps showing two distinct memory states with low and high values of both capacitance and conductance. Such admittance-voltage loops demonstrated well-defined squareness. One can conclude, that the admittance signal measurements allow definition of memory windows also for such materials which possess too high conductivity to allow switching between the low and high resistance states in the conventional measurements.

## Acknowledgements

The study was partially supported by the Finnish Centre of Excellence in Atomic Layer Deposition (284623), Spanish Ministry of Economy and Competitiveness and the FEDER program (TEC2017-84321-C4-2-R), and Estonian Academy of Sciences.

## References:

- [1] Ghazaryan L, Kley, E-B, Tünnermann A and Szeghalmi A 2016 Nanoporous SiO<sub>2</sub> thin films made by atomic layer deposition and atomic etching *Nanotechnology* **27** 255603 <http://dx.doi.org/10.1088/0957-4484/27/25/255603>
- [2] Francisco M S P, Gushikem Y, 2002 Synthesis and characterization of SiO<sub>2</sub>–Nb<sub>2</sub>O<sub>5</sub> systems prepared by the sol–gel method: structural stability studies *J. Mater. Chem.* **12** 2552–2558. <https://doi.org/10.1039/b200685e>
- [3] Umpierres C. S, Prola L D T, Adebayo M A, Lima E C, dos Reis G S, Kunzler D D F, Dotto G L, Arenas L T, and Benvenuti E V 2017 Mesoporous Nb<sub>2</sub>O<sub>5</sub>/SiO<sub>2</sub> material obtained by sol–gel method and applied as adsorbent of crystal violet dye *Environ. Technol.* **38** 566–578 <https://doi.org/10.1080/09593330.2016.1202329>
- [4] Leitel R, Stenzel O, Wilbrandt S, Gäbler D, Janicki V and Kaiser N 2006 Optical and non-optical characterization of Nb<sub>2</sub>O<sub>5</sub>–SiO<sub>2</sub> compositional graded-index layers and rugate structures *Thin Solid Films* **497**, 135–141 <http://dx.doi.org/10.1016/j.tsf.2005.10.064>
- [5] Ullah A, Wilke H, Memon I, Shen Y, Nguyen, D T, Woitdt C and Hillmer H 2015 Stress relaxation in dual ion beam sputtered Nb<sub>2</sub>O<sub>5</sub> and SiO<sub>2</sub> thin films: application in a Fabry–Pérot filter array with 3D nanoimprinted cavities *J. Micromech. Microeng.* **25**, 055019 <http://dx.doi.org/10.1088/0960-1317/25/5/055019>
- [6] Wang G, Yang Y, Lee J-H, Abramova V, Fei H, Ruan, G, Thomas E L and Tou J M 2014 Nanoporous silicon oxide memory *Nano Lett.* **14**, 4694–4699 <http://dx.doi.org/10.1021/nl501803s>
- [7] Wang Y, Liu Q, Lv H-B, Long S-B, Zhang S, Li Y-T, Lian W-T, Yang J-H and Liu M 2011 CMOS compatible nonvolatile memory devices based on SiO<sub>2</sub>/Cu/SiO<sub>2</sub> multilayer films *Chin. Phys. Lett.* **28**, 077201 <http://dx.doi.org/10.1088/0256-307X/28/7/077201>
- [8] Janicki V, Sancho-Parramon J, Yulin S, Flemming M and Chuvilin A 2012 Optical and structural properties of Nb<sub>2</sub>O<sub>5</sub>–SiO<sub>2</sub> mixtures in thin films, *Surf. Coat. Technol.* **206**, 3650–3657 <http://dx.doi.org/10.1016/j.surfcoat.2012.03.015>
- [9] Richter F, Kupfer H, Schlott P, Gessner T and Kaufmann, C 2001 Optical properties and mechanical stress in SiO<sub>2</sub>–Nb<sub>2</sub>O<sub>5</sub> multilayers. *Thin Solid Films* **389**, 278–283 [https://doi.org/10.1016/S0040-6090\(01\)00864-1](https://doi.org/10.1016/S0040-6090(01)00864-1)
- [10] Lee C-C, Tien C-L and Hsu J-C 2002 Internal stress and optical properties of Nb<sub>2</sub>O<sub>5</sub> thin films deposited by ion-beam sputtering. *Appl. Opt.* **41**, 2043 <https://doi.org/10.1364/AO.41.002043>
- [11] Melninkaitis A, Tolenis T, Mažulė L, Mirauskas J, Sirutkaitis V, Mangote B, Fu X, Zerrad M, Gallais L, Commandré M, Kičas S and Drazdys R 2011 Characterization of zirconia–and niobia–silica mixture coatings produced by ion-beam sputtering *Appl. Opt.* **50**, C188–C196 <https://doi.org/10.1364/AO.50.00C188>

- [12] Jiang H, Li X Y, Chen R, Shao X L, Yoon J H, Hu X, Hwang C S and Zhao J 2016 Bias-polarity-dependent resistance switching in W/SiO<sub>2</sub>/Pt and W/SiO<sub>2</sub>/Si/Pt structures. *Sci. Rep.* **6**, 22216 <http://dx.doi.org/10.1038/srep22216>
- [13] Wu J, Ye C, Zhang J, Deng T, He P and Wang H 2016 Multilevel characteristics for bipolar resistive random access memory based on hafnium doped SiO<sub>2</sub> switching layer. *Mater. Sci. Semicond. Proc.* **43**, 144–148. <https://doi.org/10.1016/j.mssp.2015.12.012>
- [14] Wu F, Si S, Shi T, Zhao X, Liu Q, Liao L, Lv H, Long S and Liu M 2018 Negative differential resistance effect induced by metal ion implantation in SiO<sub>2</sub> film for multilevel RRAM application *Nanotechnology* **29**, 054001. <https://doi.org/10.1088/1361-6528/aaa065>
- [15] Cheng C-H, Chou K I, Zheng Z-W and Hsu H-H 2014 Low power resistive random access memory using interface-engineered dielectric stack of SiO<sub>x</sub>/a-Si/TiO<sub>y</sub> with 1D1R-like structure *Curr. Appl. Phys.* **14**, 139-143 <https://doi.org/10.1016/j.cap.2013.10.019>
- [16] Liu C-Y, Huang J-J and Lai C-H 2013 Resistive switching characteristics of a Pt nanoparticle-embedded SiO<sub>2</sub>-based memory *Thin Solid Films* **529**, 107–110 <http://dx.doi.org/10.1016/j.tsf.2012.03.108>
- [17] Chang Y-F, Feng L-W and Chang T.-C. 2011 Mechanism and characterizations studies of resistive switching effects on a thin FeO<sub>x</sub>-transition layer of the Ti/TiN/SiO<sub>2</sub>/FeO<sub>x</sub>/FePt structure by thermal annealing treatments *Mater. Chem. Phys.* **131**, 262–267 <https://doi.org/10.1016/j.matchemphys.2011.09.037>
- [18] Matero R, Haukka S and Tuominen M. 2008 High growth rate SiO<sub>2</sub> by atomic layer deposition. *ECS Transact.* **13**, 453-457 <http://dx.doi.org/10.1149/1.2911529>
- [19] Tomczak Y, Knapas K, Haukka, S, Kemell M, Heikkilä M, Ceccato M, Leskelä M, and Ritala M. 2012 *In situ* reaction mechanism studies on atomic layer deposition of Al<sub>x</sub>Si<sub>y</sub>O<sub>z</sub> from trimethylaluminium, hexakis(ethylamino)disilane, and water. *Chem. Mater.* **24**, 3859–3867 <http://dx.doi.org/10.1021/cm301658m>
- [20] Fuschillo N, Lalevic B and Annamalai N K 1975 Dielectric properties of amorphous Nb<sub>2</sub>O<sub>5</sub> thin films *Thin Solid Films* **30**, 145-154 [https://doi.org/10.1016/0040-6090\(75\)90316-8](https://doi.org/10.1016/0040-6090(75)90316-8)
- [21] Blanquart T, Niinistö J, Heikkilä M, Sajavaara T, Kukli, K, Puukilainen E, Xu C, Hunks W, Ritala M and Leskelä M 2012 Evaluation and comparison of novel precursors for atomic layer deposition of Nb<sub>2</sub>O<sub>5</sub> thin films *Chem. Mater.* **24**, 975–980 <https://doi.org/10.1021/cm2026812>
- [22] Yamato M, Tanioku M, Hara H and Kikkawa T. 2008 Properties of Al<sub>2</sub>O<sub>3</sub>/Nb<sub>2</sub>O<sub>5</sub> and Ta<sub>2</sub>O<sub>5</sub>/Nb<sub>2</sub>O<sub>5</sub> stacked and mixed films for gigabit DRAM capacitor, *Int. Conf. Solid State Dev. Mater.* 232-233 <https://doi.org/10.7567/SSDM.2008.J-1-6>
- [23] Clima S, Pourtois G, Van Elshocht S, De Gendt, S, Heyns M, Wouters D J and Kittl J A 2009 Dielectric response of Ta<sub>2</sub>O<sub>5</sub>, NbTaO<sub>5</sub> and Nb<sub>2</sub>O<sub>5</sub> from first-principles investigations *ECS Transact.* **19**, 729-737 <https://doi.org/10.1149/1.3122128>

- [24] Cho K, Lee J, Lim J-S, Lim H, Lee, Moon J-T, Park, S J, Yoo C-Y, Kim S-T and Chung U-I 2005 Low temperature crystallized Ta<sub>2</sub>O<sub>5</sub>/Nb<sub>2</sub>O<sub>5</sub> bi-layers integrated into RIR capacitor for 60 nm generation and beyond *Microel. Eng.* **80**, 317-320  
<https://doi.org/10.1016/j.mee.2005.04.032>
- [25] Wang L-G, Qian X, Cao Y-Q, Cao Z-Y, Cao Z-Y, Fang G-Y, Li, A-D and Wu D 2015 Excellent resistive switching properties of atomic layer-deposited Al<sub>2</sub>O<sub>3</sub>/HfO<sub>2</sub>/Al<sub>2</sub>O<sub>3</sub> trilayer structures for non-volatile memory applications, *Nanoscale Res. Lett.* **10**, 135.  
<https://doi.org/10.1186/s11671-015-0846-y>
- [26] Huang C-Y, Huang C-Y, Tsai T-L, Lin C-A and Tseng T-Y 2014 Switching mechanism of double forming process phenomenon in ZrO<sub>x</sub>/HfO<sub>y</sub> bilayer resistive switching memory structure with large endurance, *Appl. Phys. Lett.* **104**, 062901.  
<http://dx.doi.org/10.1063/1.4864396>
- [27] Huang X, Wu H, Gao B, Sekar D C, Dai L, Kellam M, Gary Bronner G, Deng N and Qian H 2016 HfO<sub>2</sub>/Al<sub>2</sub>O<sub>3</sub> multilayer for RRAM arrays: a technique to improve tail-bit retention, *Nanotechnology* **27**, 395201 <https://doi.org/10.1088/0957-4484/27/39/395201>
- [28] Siles P F, de Pauli M, Bufon C C B, Ferreira S O, Bettini J, Schmidt O G and Malachias, A 2013 Tuning resistive switching on single-pulse doped multilayer memristors, *Nanotechnology* **24**, 035702. <https://doi.org/10.1088/0957-4484/24/3/035702>
- [29] Sokolov A S, Son S K, Lim D, Han H H, Jeon Y-R, Lee J H, Choi C 2017 Comparative study of Al<sub>2</sub>O<sub>3</sub>, HfO<sub>2</sub>, and HfAlO<sub>x</sub> for improved self-compliance bipolar resistive switching, *J. Am. Ceram Soc.* **100**, 5638 – 5648. <http://dx.doi.org/10.1111/jace.15100>
- [30] Bayat F, Prezioso M, Chakrabarti B, Nili H, Kataeva I and Strukov D 2018 Implementation of multilayer perceptron network with highly uniform passive memristive crossbar circuits, *Nature Communications* **9**, 2331  
<http://dx.doi.org/10.1038/s41467-018-04482-4>
- [31] Park G-S, Kim Y B, Park S Y, Li X S, Heo S, Lee M-J, Chang M, Kwon J H, Kim, M, Chung U-I, Dittmann R, Waser R and Kim K 2013 In situ observation of filamentary conducting channels in an asymmetric Ta<sub>2</sub>O<sub>5-x</sub>/TaO<sub>2-x</sub> bilayer structure, *Nature Comm.* **4**, 2382 <https://doi.org/10.1038/ncomms3382>
- [32] Sathasivam S, Williamson B A D, Althabaiti S A, Obaid A Y, Basahel S N, Mokhtar M, Scanlon D O, Carmalt C J and Parkin I P 2017 Chemical vapor deposition synthesis and optical properties of Nb<sub>2</sub>O<sub>5</sub> thin films with hybrid functional theoretical insight into the band structure and band gaps, *ACS Appl. Mater. Interfaces* **9**, 18031–18038  
<http://dx.doi.org/10.1021/acsami.7b00907>
- [33] Pickett M D, Medeiros-Ribeiro G and Williams R S 2012 A scalable neuristor built with Mott memristors, *Nature Materials* **12**, 114-117 <http://dx.doi.org/10.1038/NMAT3510>
- [34] Nagata T, Haemori, M, and Chikyow T 2013 Combinatorial synthesis of Cu/(Ta<sub>x</sub>Nb<sub>1-x</sub>)<sub>2</sub>O<sub>5</sub> stack structure for nanoionics-type ReRAM device, *ACS Comb. Sci.* **15**, 435–438  
<http://dx.doi.org/10.1021/co4000425>

- [35] Wylezich H, Mähne H, Rensberg J, Ronning C, Zahn P, Slesazeck S and Mikolajick T 2014 Local ion irradiation-induced resistive threshold and memory switching in Nb<sub>2</sub>O<sub>5</sub>/NbO<sub>x</sub> films *ACS Appl. Mater. Interfaces* **6**, 17474–17480 <http://dx.doi.org/10.1021/am5021149>
- [36] Wylezich H, Reinhardt E, Slesazeck S and Mikolajick T 2015 Integration of niobium oxide-based resistive switching cells with different select properties into nanostructured cross-bar arrays. *Semicond. Sci. Technol.* **30**, 115014 <http://dx.doi.org/10.1088/0268-1242/30/11/115014>
- [37] Kundozerova T V, Grishin A M, Stefanovich G B and Velichko A A 2012 Anodic Nb<sub>2</sub>O<sub>5</sub> nonvolatile RRAM. *IEEE Transact. Electron Dev.* **59**, 1144–1148 <http://dx.doi.org/10.1109/TED.2011.2182515>
- [38] Baek H, Lee C, Choi J and Cho J 2013 Nonvolatile memory devices prepared from sol-gel derived niobium pentoxide films *Langmuir* **29**, 380–386 <https://doi.org/10.1021/la303857b>
- [39] Min Kim K, Zhang J, Graves C, Yang J J, Choi B J, Hwang C S, Li Z and Williams, R S 2016 Low-power, self-rectifying, and forming-free memristor with an asymmetric programming voltage for a high-density crossbar application. *Nano Lett.* **16**, 6724–6732 <http://dx.doi.org/10.1021/acs.nanolett.6b01781>
- [40] Santamaria M, Di Franco F, Di Quarto F, Skeldon P and Thompson, G. E. 2013 Tailoring of the solid state properties of Al – Nb mixed oxides: A photoelectrochemical study *J. Phys. Chem. C* **117**, 4201–4210 <http://dx.doi.org/10.1021/jp312008m>
- [41] Xu Y, Chen L, Sun Q-Q, Gu J-J, Lu H-L, Wang P-F, Ding S-J and Zhang D W 2010 Electronic structure and optical properties of Nb doped Al<sub>2</sub>O<sub>3</sub> on Si by atomic layer deposition *Solid State Comm.* **150**, 1690–1692 <http://dx.doi.org/10.1016/j.ssc.2010.06.023>
- [42] Kukli K, Ritala M, Leskelä M and Lappalainen R. 1998 Niobium oxide thin films grown by atomic layer epitaxy *Chem. Vap. Deposition* **4**, 29–34. [https://doi.org/10.1002/\(SICI\)1521-3862\(199801\)04:01<29::AID-CVDE29>3.0.CO;2-R](https://doi.org/10.1002/(SICI)1521-3862(199801)04:01<29::AID-CVDE29>3.0.CO;2-R)
- [43] Knapas K, Rahtu A and Ritala M 2010 Reaction mechanism studies on atomic layer deposition of Nb<sub>2</sub>O<sub>5</sub> from Nb(OEt)<sub>5</sub> and water *Langmuir* **26**, 848–853 <http://dx.doi.org/10.1021/la902289h>
- [44] Ouendi S, Arico C, Blanchard F, Codron J-L, Wallart X, Taberna P-L, Roussel P, Clavier L, Simon P, Lethien C 2019 Synthesis of T-Nb<sub>2</sub>O<sub>5</sub> thin-films deposited by atomic layer deposition for miniaturized electrochemical energy storage devices. *Energy Storage Mater.* **16**, 581–588 <http://dx.doi.org/10.1016/j.ensm.2018.08.022>
- [45] Chen L, Sun Q-Q, Gu J-J, Xu Y, Ding S-J, Zhang D W 2011 Bipolar resistive switching characteristics of atomic layer deposited Nb<sub>2</sub>O<sub>5</sub> thin films for nonvolatile memory application *Curr. Appl. Phys.* **11**, 849–852 <http://dx.doi.org/10.1016/j.cap.2010.12.005>

- [46] Mehonic A, Shluger L A, Gao D, Valov I, Miranda E, Ielmini D, Bricalli A, Ambrosi E, Li C, Yang J J, Xia Q and Kenyon J A 2018 Silicon oxide (SiO<sub>x</sub>): A Promising Material for Resistance Switching? *Adv. Mater.* **30**, <http://dx.doi.org/10.1002/adma.201801187>
- [47] Mehonic A, Cuffe S, Wojdak M, Hudziak S, Jambois O, Labbé C, Garrido B, Rizk R and Kenyon, J A 2012 Resistive switching in silicon suboxide films *J. Appl. Phys.* **111**, 074507. <http://dx.doi.org/10.1063/1.3701581>
- [48] Hong X, Loy D J, Dananjaya P A, Tan F, Ng C and Lew W 2018 Oxide-based RRAM materials for neuromorphic computing *J. Mater. Sci.* **53**, 8720–8746 <https://doi.org/10.1007/s10853-018-2134-6>
- [49] Chang K-C, Huang J-W, Chang T-C, Tsai T-M, Chen K-H, Young T-F, Chen J-H, Zhang R, Lou J-C, Huang S-Y, Pan Y-C, Huang H-C, Syu Y-E, Gan D-S, Bao D-H and Sze S M 2013 Space electric field concentrated effect for Zr:SiO<sub>2</sub> RRAM devices using porous SiO<sub>2</sub> buffer layer *Nanoscale Res. Lett.* **8**:523 <http://www.nanoscalereslett.com/content/8/1/523>
- [50] Suntola T 1992 Atomic layer epitaxy *Thin Solid Films* **216**, 84-89 [http://dx.doi.org/10.1016/0040-6090\(92\)90874-B](http://dx.doi.org/10.1016/0040-6090(92)90874-B)
- [51] Vignaud G and Gibaud A 2019 REFLEX: a program for the analysis of specular X-ray and neutron reflectivity data *J. Appl. Cryst.* **52**, 201-213 <https://doi.org/10.1107/S1600576718018186>
- [52] Waldo R A 1988 Microbeam Analysis, San Francisco Press, San Francisco, CA, pp. 310
- [53] Jokinen J, Keinonen J, Tikkanen P, Kuronen A, Ahlgren T and Nordlund K 1996 Comparison of TOF-ERDA and nuclear resonance reaction techniques for range profile measurements of keV energy implants *Nucl. Inst. Met. Phys. Res. B* **119**, 533-542 [http://dx.doi.org/10.1016/S0168-583X\(96\)00469-7](http://dx.doi.org/10.1016/S0168-583X(96)00469-7)
- [54] Spiga D, Mirone A, Pareschi G, Canestrari R, Cotroneo V, Ferrari C, Ferrero C, Lazzarini L and Vernani D 2006 Characterization of multilayer stack parameters from X-ray reflectivity data using the PPM program: measurements and comparison with TEM results *Proc. SPIE 6266, Space Telescopes and Instrumentation II: Ultraviolet to Gamma Ray* 626616 <http://dx.doi.org/10.1117/12.672895>
- [55] Sintonen S, Ali S, Ylivaara O M E, Puurunen R L and Lipsanen H 2014 X-ray reflectivity characterization of atomic layer deposition Al<sub>2</sub>O<sub>3</sub>/TiO<sub>2</sub> nanolaminates with ultrathin bilayers *J. Vac. Sci. Technol. A* **32**, 01A111 <http://dx.doi.org/10.1116/1.4833556>
- [56] Jensen J M, Oelkers A B, Toivola R, Johnson D C, Elam J W and George S M 2002 X-ray reflectivity characterization of ZnO/Al<sub>2</sub>O<sub>3</sub> multilayers prepared by atomic layer deposition *Chem. Mater.* **14**, 2276–2282 <http://dx.doi.org/10.1021/cm011587z>
- [57] Lee J and Park S 2016 Systematic determination of the thickness of a thin oxide layer on a multilayered structure by using an X-ray reflectivity analysis. *J. Korean Phys. Soc.* **69**, 789-792 <http://dx.doi.org/10.3938/jkps.69.789>



- [58] Dueñas S, Castán H, García H, Ossorio Ó G, Domínguez L A and Miranda E 2017 Experimental observation of negative susceptance in HfO<sub>2</sub>-based RRAM devices. *IEEE Electron Dev. Lett.* **38**, 1216-1219 <https://doi.org/10.1109/LED.2017.2723054>
- [59] Dueñas S, Castán H, Kukli K, Mikkor M, Kalam K, Arroval T and Tamm A 2018 Memory maps: Reading RRAM devices without power consumption *ECS Transact.* **85**, 201-2015 <https://doi.org/10.1149/08508.0201ecst>
- [60] Tian M and Zhong H 2019 Effects of electrode on the performance of Al<sub>2</sub>O<sub>3</sub> based metal-insulator-metal antifuse *ECS J. Solid State Sci. Technol.* **8**, N32-N35. <https://doi.org/10.1149/2.0071902jss>